

# Experimental network advantage for quantum conference key agreement

Alexander Pickston<sup>†,1</sup>, Joseph Ho<sup>†,1</sup>, Andrés Ulibarrena,<sup>1</sup> Federico Grasselli,<sup>2</sup> Massimiliano Proietti,<sup>1</sup> Christopher L. Morrison,<sup>1</sup> Peter Barrow,<sup>1</sup> Francesco Graffiti,<sup>1</sup> and Alessandro Fedrizzi<sup>1</sup>

<sup>1</sup>*Institute of Photonics and Quantum Sciences, School of Engineering and Physical Sciences, Heriot-Watt University, Edinburgh EH14 4AS, United Kingdom*

<sup>2</sup>*Institut für Theoretische Physik III, Heinrich-Heine-Universität Düsseldorf, Universitätsstraße 1, D-40225 Düsseldorf, Germany*

One of the great promises of quantum technology is the development of quantum networks, which will allow global distribution of entanglement for tasks such as distributed quantum computing [1, 2], distributed quantum sensing [3, 4] and quantum-secure communication [5–8]. To leverage the full potential of quantum networks we require protocols that draw an efficiency advantage from genuine multi-partite entanglement as opposed to strictly pair-wise correlations such as Bell states. Multi-user entanglement such as Greenberger-Horne-Zeilinger (GHZ) states have already found application in quantum conference key agreement [9–12], quantum secret sharing [13–15] and quantum communication complexity problems [16, 17]. However, a true network advantage has not yet been achieved. In this work we create a six-photon graph-state network from which we derive either a four-user GHZ state for direct quantum conference key agreement [18–21] or the required amount of Bell pairs for the equivalent pair-wise protocol. We show that the GHZ-state protocol has a more than two-fold rate advantage by only consuming half the amount of network resources per secure conference key bit.

In quantum conference key agreement (QCKA),  $N$  users aim to establish a common and identical secret key for group-wide encryption. There are two main approaches to achieve this when the group of users are connected in a network as depicted in Figure 1. The first method involves obtaining bi-partite entangled states from which secure pair-wise keys are generated using standard QKD [22]. This set of keys can then be used to produce the conference key by performing a bit-wise XOR operation on the individual keys—we will refer to this as the ‘2QKD’ approach. A more resource-efficient method, referred to as ‘NQKD’, leverages multi-partite entanglement to obtain the conference key directly from a GHZ state supplied to all participating users. This approach can outperform the 2QKD scheme by consuming up to  $N-1$  fewer network resources in constrained quantum networks [9, 23]. QCKA was recently demonstrated in a four-user NQKD scenario where a four-photon GHZ state was directly transmitted over up to 50 km of telecom fibre [12]. However, a direct comparison showing the experimental resource advantage over the 2QKD approach in a quantum network has not yet been achieved.

In this work we demonstrate a genuine network advantage of QCKA when exploiting multi-partite entanglement by using a six-photon graph state to emulate a non-trivially connected six-user network. We use the graph state shown in Figure 1 and so-called network coding techniques [20, 24, 25], which involve local operations,

quantum measurements and classical communication to alter the connectivity of the network. This allows network users to conduct the two alternative QCKA techniques to reveal the direct resource advantage of using a multi-partite protocol.

For the NQKD approach we consider the N-BB84 protocol [10] that was implemented in Ref. [12]. In each protocol round, an  $N$ -partite GHZ state is distributed among  $N$  users. Each user performs a measurement on their respective qubit according to a pre-agreed sequence of two possible measurements. In type-1 rounds each user measures their qubit in the Pauli Z-basis, exploiting the perfect Z-correlations for generation of the raw key; type-2 rounds correspond to jointly measuring in X and are used for parameter estimation. Security is established by evaluating  $Q_X$  from the type-2 rounds and determining the quantum bit error rate (QBER) from a random subset of publicly disclosed type-1 outcomes. We can assess the performance of the N-BB84 protocol, in the limit of an infinite number of rounds, by determining these two parameters and calculating the asymptotic key rate (AKR) [10, 12]. The AKR establishes the fractional secret key bit extracted for each copy of the resource state and is defined as,

$$\text{AKR} = 1 - H(\text{QBER}) - H(Q_X), \quad (1)$$

where  $H(x) \doteq -x \log_2(x) - (1-x) \log_2(1-x)$  is the binary entropy function. The explicit evaluation of QBER and  $Q_X$  is detailed in the Appendix.

In the case of 2QKD, users initially obtain sets of Bell states, rather than a GHZ state, from which they run

<sup>†</sup> These two authors contributed equally.

\* Corresponding author: a.fedrizzi@hw.ac.uk

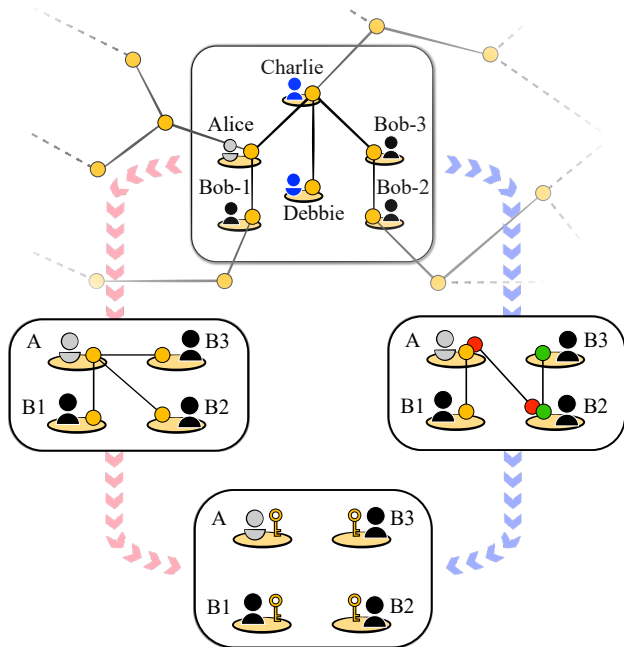


FIG. 1. **Conceptual illustration of a multi-node quantum network.** Physical qubits are represented by nodes (circles), while edges (lines) represent pair-wise interactions that entangle the qubits within the wider network. Here, we define a subnetwork consisting of six users represented by nodes within the rounded rectangle. Within this subnetwork, four of the users may wish to perform quantum protocols such as conference key agreement. The traditional method involves distributing Bell pairs among the participants first, followed by post-processing steps to extract keys in a pairwise fashion before arriving at the final conference key as shown by the right path in blue. An alternative approach is to obtain a GHZ state and employ a multi-party quantum conference key agreement protocol to extract the key directly, as represented in the left red path.

pairwise BB84 protocols whose AKR is also given by the expression in (1). However, unlike in the NQKD approach, the 2QKD method involves obtaining  $N-1$  unique, pairwise keys spanning the  $N$ -user group first. This is followed by a classical step, e.g., applying the bit-wise XOR, to transform the individual keys into the final conference key [9]. As we will show in our experiment, depending on the underlying topology of the quantum network, this leads to the 2QKD approach requiring up to  $N-1$  times more network resource states than NQKD.

We experimentally prepare the six-photon graph state using a linear optical setup containing three photon-pair sources, see Appendix for details. In Figure 2(a) we outline the general layout of the sources, two-qubit Fusion gates and single-qubit rotations. Two of the sources produce Bell states,  $|\Phi^+\rangle$ , while the third generates a biseparable state with each photon encoded as  $|+\rangle$ . We arrive at the six-photon graph state by applying the set of two-qubit Fusion gates and single-qubit operations, where  $H$  and  $Z$  denote the Hadamard and Pauli-Z gates. In

our setup we use probabilistic two-qubit fusion gates [26] which have a success rate of  $1/2$  per gate. This leads to an overall probability of obtaining the target six-photon state as  $P_s = 1/8$ , conditional on detecting one photon in each mode.

We adopt the graph state formalism [24] to represent the six-photon state. This representation allows us to exploit techniques for transforming the underlying entanglement structure, via local complementation (LC) [20, 24, 25], as shown in Figure 2(b). We illustrate how LC operations on the six-photon graph results in a four-party GHZ state in modes  $\{1, 2, 5, 6\}$ , corresponding to four users, e.g., Alice, Bob-1, Bob-2 and Bob-3, implementing NQKD. Conventionally, Alice denotes the party who co-ordinates the error correction and privacy amplification steps after the raw key is established [9, 10, 12]. We also include LC operations mapped to sets of single-qubit gates [25] in the circuit. Nodes 3 and 4 represent users Charlie and Debbie, who do not participate in the QCKA key generation. They measure their qubits in the Z basis then announce their outcomes, which allows the qubits to be coherently removed from the graph. The remaining four qubits are transformed into the star graph which is a locally equivalent to the four-party GHZ state [24] required for the NQKD protocol. We then construct measurement sequences consistent with type-1 and type-2 rounds, i.e.,  $Z^{\otimes 4}$  and  $X^{\otimes 4}$  respectively, of the NQKD protocol.

The method for transforming the six-photon state into Bell pairs for the 2QKD protocol is outlined in Figure 2(c). To generate a conference key among the four users, at least three pairwise keys are required. There are two sets of network transformations for obtaining three individual Bell pairs among the same group of four users that participated in the NQKD protocol. On the top of Figure 2(c) we show how to obtain Bell pairs between nodes  $\{1, 2\}$  and  $\{5, 6\}$  respectively from a single copy of the six-photon resource graph state. While the bottom of the same figure shows a single Bell pair established between modes  $\{2, 5\}$ . We similarly construct the measurement sequences corresponding to type-1 and type-2 rounds for each Bell pair, see Appendix for details.

The outcomes of type-1 and type-2 rounds are used to calculate the noise parameters  $Q_{BER}$  and  $Q_X$  which are then used to evaluate the AKR using the expression in (1). This expression corresponds to the asymptotic conference key rate for the NQKD approach and we denote it as  $AKR_N$ . While for the 2QKD approach, (1) first computes the pairwise AKR of each BB84 protocol, denoted  $\{r_{AB_1}, r_{B_2B_3}, r_{AB_2}\}$ ; the resulting asymptotic conference key rate is then obtained using the expression,

$$AKR_2 = \frac{1}{\frac{1}{r_{AB_2}} + \max\left\{\frac{1}{r_{AB_1}}, \frac{1}{r_{B_2B_3}}\right\}}. \quad (2)$$

In the ideal case where the AKR of each Bell pair is unity,

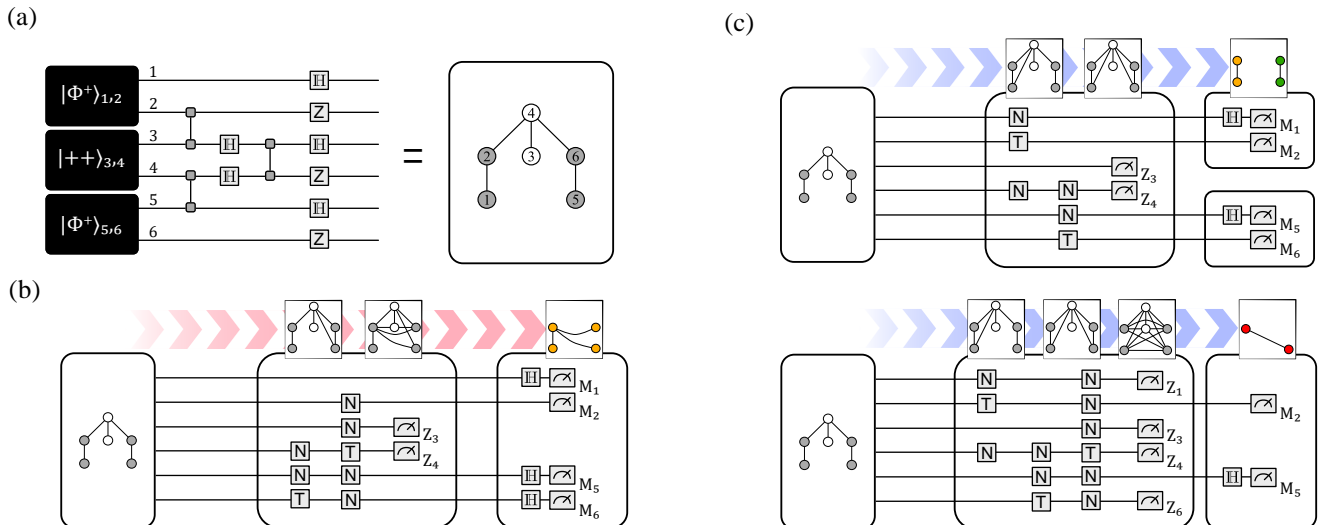


FIG. 2. **Experimentally generating and manipulating the six-photon graph state.** (a) On the left is the linear optical circuit for generating the target graph state on the right. Three photon-pair sources are represented as black boxes with each horizontal line representing a labelled optical mode containing one photon. Two sources produce Bell states,  $|\Phi^+\rangle$ , while the third generates a biseparable state with each photon in  $|+\rangle$ . The two-qubit fusion gates are denoted by two squares on the modes they act upon connected by a vertical line. Single-qubit operations, i.e., Hadamard and Pauli-Z gates are shown as squares with letters H and Z respectively. (b) The set of graph transformations for obtaining the four-qubit GHZ state, in modes  $\{1, 2, 5, 6\}$ , are depicted in the red path. This corresponds to local operations consisting of single-qubit gates  $N \doteq \sqrt{-iX}$  and  $T \doteq \sqrt{iZ}$ , where X and Z are again Pauli gates, followed by quantum measurements on non-participatory qubits  $\{3, 4\}$  in the Z basis. The remaining qubits can be measured in the joint-Z or-X basis allowing us to evaluate the key rate performance for the NQKD method. (c) We outline the two sets of local-graph operations for obtaining the three Bell pairs which are needed for the 2QKD approach.

we obtain  $\text{AKR}_2^{\text{ideal}} = 1/2$  while for the NQKD case with an ideal four-party GHZ state we can attain  $\text{AKR}_N^{\text{ideal}} = 1$ . The expected ratio of the key rate advantage in favour of NQKD is therefore  $\text{AKR}_N^{\text{ideal}} : \text{AKR}_2^{\text{ideal}} = 2$  given our specific six-photon graph. This advantage originates from the ability to use a single copy of the six-photon graph state to produce one secure bit of the conference key via NQKD, whereas in 2QKD each secure bit requires two copies of the network graph state.

We compare the experimental results of type-1 and type-2 measurements for both approaches in Figure 3. We set the pump power to each source to obtain an average six-photon detection rate of  $\sim 0.0141$  Hz for all measurements. This optical pumping regime was chosen to limit multi-photon events while still ensuring sufficient detection rates to collect statistics for each protocol, for details on the effect of optical pump parameters see Supplementary Materials. From the data in Figure 3 we calculate QBER and  $Q_X$ , for each resource state. We then evaluate the asymptotic conference key rate for NQKD,  $\text{AKR}_N = 0.093(22)$  and for 2QKD,  $\text{AKR}_2 = 0.044(15)$ . We arrive at the experimentally measured ratio of the two approaches to be  $\text{AKR}_N^{\text{exp}} : \text{AKR}_2^{\text{exp}} = 2.13(6)$ . The uncertainties reported here are taken as one standard deviation from the average of samples via a Monte Carlo simulation which assumes Poissonian counting statistics.

Noise distributed unevenly between qubits leads to different pairwise key rates for the 2QKD approach. In turn, this leads to a larger maximum in the denominator of (2) resulting in a decrease of the 2QKD conference key rate. Meanwhile, for the NQKD approach we remark that QBER is set by the largest pair-wise error rate with respect to a common user, typically labelled as Alice [10]:  $\text{QBER} \doteq \max_i \{Q_{AB_i}\}$ . However, since the NQKD protocol is symmetric with respect to permutations of the parties' roles, choosing which party is labelled as Alice can be delayed to the classical post-processing phase, allowing for an optimal choice which minimises the QBER and hence maximises  $\text{AKR}_N$ .

We have demonstrated that QCKA performed on our graph-state quantum network derives an above two-fold rate advantage from multi-party entanglement when compared to Bell states generated from the same network. Distributing GHZ states directly for NQKD will struggle to outperform much faster state-of-the-art point-to-point QKD systems [22, 27], as loss scales exponentially with the number of transmitted photons [28, 29]. However, once genuine quantum networks which generate large-scale entanglement in the background become available, NQKD outperforms 2QKD in terms of key rate per network use as we have demonstrated here.

In principle, NQKD can achieve an  $N - 1$ , i.e., three-

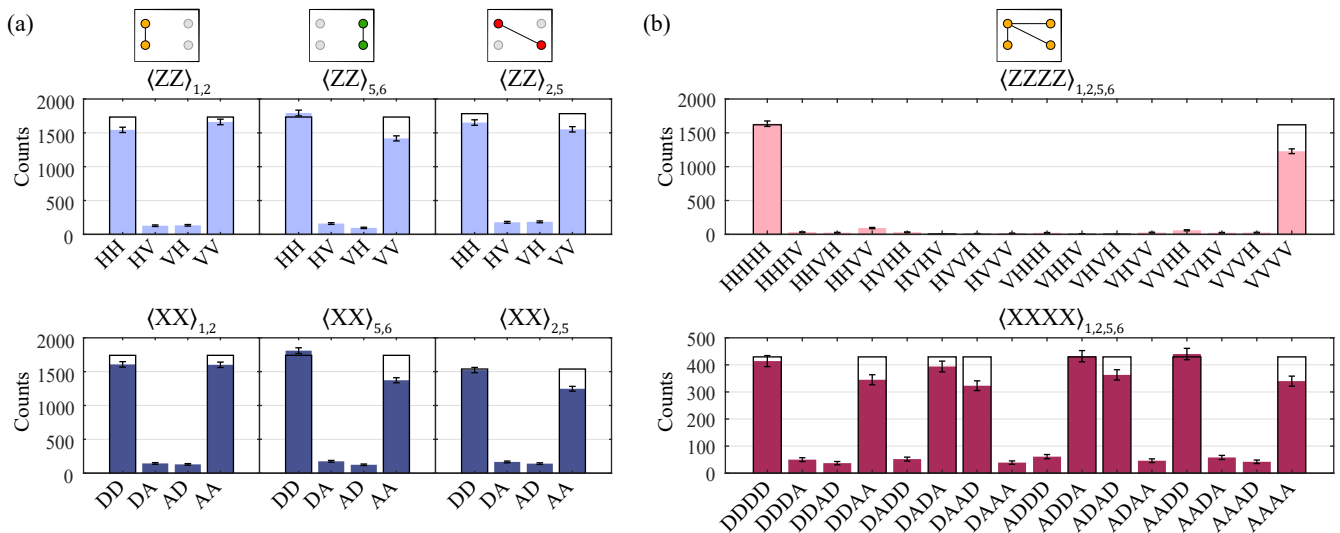


FIG. 3. Experimentally measured populations of (a) three Bell pairs used for 2QKD and (b) the four-party GHZ state for NQKD. The type-1 rounds are shown in the top set of measurements, while type-2 rounds are shown in the bottom set. These outcomes are extracted from complete measurements in the six-photon state space, wherein post-selection of the non-participatory nodes have taken place. The theoretically expected populations are included as transparent bars. All measurements are recorded for the same integration time at a fixed optical pump power and error bars are shown for one standard deviation assuming Poissonian statistics.

fold advantage in our four-user scenario. However, our specific graph allows for a Bell state *multi-cast* [9], where more than one Bell pair can be shared from a single network resource between participating users. The 2QKD rate is therefore boosted by 50%. While NQKD will still always retain an advantage, the option of multi-casting needs to be taken into account for rate comparisons in other network topologies. In the Supplementary Discussion we investigate this for the six-photon graph that corresponds to the canonical ‘butterfly’ network.

Another aspect where NQKD seems to have an advantage over 2QKD, which is worth further quantification, is in key post-processing. When evaluating our secure NQKD rates, we made use of the fact that the protocol allows for pairwise error rates to be evaluated for all permutations of the conference group, with Alice being designated based on minimising the overheads lost in error correction. A similar optimisation for 2QKD would require a-priori channel estimation, and thus additional network resources, to establish the optimal user pairs for Bell state distribution. Note that the NQKD rate advantage receives a further slight boost once finite key effects are considered, as previously noted in Ref [12].

As one of the first multi-user quantum communication protocols with a network advantage, QCKA is now a very active research area. Protocols have been developed for measurement-device independent scenarios [30] and implementations with weak coherent states that might outperform N-photon GHZ state transmission [31]. Studies of QCKA have raised fundamental questions about the type of entanglement that is useful in multi-user quan-

tum communication. It has been shown that genuine multi-partite entanglement is not strictly required for QCKA [32]. Nonetheless, obtaining a non-zero conference key could be used as a witness for entanglement in a network [32].

It will be important to explore other protocols that gain an advantage from multi-partite entanglement in quantum networks. One example is anonymous conference key agreement which enables a conference key to be distilled while hiding the identities of the participants [33–36]. A QCKA-based variant of this protocol has theoretically been shown to gain a significant advantage when using both GHZ states and Bell pairs [34] compared to using Bell pairs alone [37]. Going beyond QCKA, quantum secret sharing [13] is a well-known multi-user cryptography task that has a provable network advantage using GHZ-state correlations in the continuous variable regime [38]. A key question for these protocols is whether the required multi-party states can be obtained from an underlying network efficiently. For networks based on graph states this has been answered in the affirmative [20] however generalisations to other resource states is an ongoing challenge [39].

### Acknowledgements

This work was supported by the UK Engineering and Physical Sciences Research Council (Grant Nos. EP/T001011/1.). F Graffitti acknowledges studentship funding from EPSRC under Grant No. EP/L015110/1. F Graselli acknowledges support from the Deutsche Forschungsgemeinschaft (DFG, German Research Foun-

ation) under Germany’s Excellence Strategy - Cluster of Excellence Matter and Light for Quantum Computing (ML4Q) EXC 2004/1 -390534769.

### Author contributions

MP, AF conceived the project. F Grasselli, AP, JH developed the theoretical framework. AP, JH, AU, CLM, F Graffitti, PB performed the experiment and collected the data. AP, JH analysed experimental data and prepared figures. All authors contributed to writing the manuscript.

### Competing interests

The authors declare no competing interests.

- 
- [1] Beals, R. *et al.* Efficient distributed quantum computing. *Proceedings of the Royal Society A: Mathematical, Physical and Engineering Sciences* **469**, 20120686 (2013). URL <https://royalsocietypublishing.org/doi/10.1098/rspa.2012.0686>.
- [2] Van Meter, R. & Devitt, S. J. The path to scalable distributed quantum computing. *Computer* **49**, 31–42 (2016). Conference Name: Computer.
- [3] Gottesman, D., Jennewein, T. & Croke, S. Longer-baseline telescopes using quantum repeaters. *Phys. Rev. Lett.* **109**, 070503 (2012). URL <https://link.aps.org/doi/10.1103/PhysRevLett.109.070503>.
- [4] Kómár, P. *et al.* A quantum network of clocks. *Nature Physics* **10**, 582–587 (2014). URL <https://www.nature.com/articles/nphys3000>.
- [5] Peev, M. *et al.* The SECOQC quantum key distribution network in Vienna. *New Journal of Physics* **11**, 075001 (2009).
- [6] Sasaki, M. *et al.* Field test of quantum key distribution in the Tokyo QKD network. *Optics express* **19**, 10387–10409 (2011).
- [7] Dynes, J. *et al.* Cambridge quantum network. *npj Quantum Information* **5**, 1–8 (2019).
- [8] Chen, T.-Y. *et al.* Implementation of a 46-node quantum metropolitan area network. *npj Quantum Information* **7**, 1–6 (2021). URL <http://www.nature.com/articles/s41534-021-00474-3>.
- [9] Epping, M., Kampermann, H., Macchiavello, C. & Bruß, D. Multi-partite entanglement can speed up quantum key distribution in networks. *New Journal of Physics* **19**, 093012 (2017). URL <https://doi.org/10.1088/1367-2630/aa8487>.
- [10] Grasselli, F., Kampermann, H. & Bruß, D. Finite-key effects in multipartite quantum key distribution protocols. *New Journal of Physics* **20**, 113014 (2018). URL <https://doi.org/10.1088/1367-2630/aaec34>.
- [11] Murta, G., Grasselli, F., Kampermann, H. & Bruß, D. Quantum conference key agreement: a review. *Advanced Quantum Technologies* **3**, 2000025 (2020). URL <http://arxiv.org/abs/2003.10186>.
- [12] Proietti, M. *et al.* Experimental quantum conference key agreement. *Science Advances* **7**, eabe0395 (2021). URL <https://advances.sciencemag.org/content/7/23/eabe0395>.
- [13] Hillery, M., Bužek, V. & Berthiaume, A. Quantum secret sharing. *Physical Review A* **59**, 1829 (1999).
- [14] Tittel, W., Zbinden, H. & Gisin, N. Experimental demonstration of quantum secret sharing. *Physical Review A* **63**, 042301 (2001).
- [15] Broadbent, A., Chouha, P.-R. & Tapp, A. The GHZ state in secret sharing and entanglement simulation. In *2009 Third International Conference on Quantum, Nano and Micro Technologies*, 59–62 (IEEE, 2009).
- [16] Buhman, H., Cleve, R., Massar, S. & De Wolf, R. Nonlocality and communication complexity. *Reviews of Modern Physics* **82**, 665 (2010).
- [17] Ho, J. *et al.* Entanglement-based quantum communication complexity beyond Bell nonlocality. *npj Quantum Information* **8**, 1–7 (2022).
- [18] Epping, M., Kampermann, H. & Bruß, D. Robust entanglement distribution via quantum network coding. *New Journal of Physics* **18**, 103052 (2016). URL <https://doi.org/10.1088/1367-2630/18/10/103052>.
- [19] Epping, M., Kampermann, H. & Bruß, D. Large-scale quantum networks based on graphs. *New Journal of Physics* **18**, 053036 (2016). URL <https://doi.org/10.1088/1367-2630/18/5/053036>.
- [20] Hahn, F., Pappa, A. & Eisert, J. Quantum network routing and local complementation. *npj Quantum Information* **5**, 1–7 (2019). URL <https://www.nature.com/articles/s41534-019-0191-6>.
- [21] Wallnöfer, J., Pirker, A., Zwerger, M. & Dür, W. Multipartite state generation in quantum networks with optimal scaling. *Scientific Reports* **9**, 1–18 (2019).
- [22] Wengerowsky, S., Joshi, S. K., Steinlechner, F., Hübel, H. & Ursin, R. An entanglement-based wavelength-multiplexed quantum communication network. *Nature* **564**, 225–228 (2018). URL <http://www.nature.com/articles/s41586-018-0766-y>.
- [23] Hahn, F., Dahlberg, A., Eisert, J. & Pappa, A. Limitations of nearest-neighbour quantum networks. *arXiv:2202.10886 [quant-ph]* (2022). URL <http://arxiv.org/abs/2202.10886>.
- [24] Hein, M., Eisert, J. & Briegel, H. J. Multi-party entanglement in graph states. *Physical Review A* **69**, 062311 (2004). URL <http://arxiv.org/abs/quant-ph/0307130>.
- [25] Adcock, J. C., Morley-Short, S., Dahlberg, A. & Silverstone, J. W. Mapping graph state orbits under local complementation. *Quantum* **4**, 305 (2020). URL <http://arxiv.org/abs/1910.03969>.
- [26] Browne, D. E. & Rudolph, T. Resource-efficient linear optical quantum computation. *Physical Review Letters* **95**, 010501 (2005). URL <https://link.aps.org/doi/10.1103/PhysRevLett.95.010501>.
- [27] Joshi, S. K. *et al.* A trusted node-free eight-user metropolitan quantum communication network. *Science Advances* **6**, eaba0959 (2020). URL <https://www.science.org/doi/full/10.1126/sciadv.aba0959>.
- [28] Singkanipa, P. & Kok, P. Quantum conference key agreement with photon loss. *arXiv preprint:2101.01483* (2021).
- [29] Takeoka, M., Guha, S. & Wilde, M. M. Fundamental rate-loss tradeoff for optical quantum key distribution. *Nature communications* **5**, 1–7 (2014).
- [30] Ottaviani, C., Lupo, C., Laurenza, R. & Pirandola, S. Modular network for high-rate quantum conferencing. *Communications Physics* **2**, 1–6 (2019). URL <https://doi.org/10.1038/s42005-019-0001-1>.

- [//www.nature.com/articles/s42005-019-0209-6](https://www.nature.com/articles/s42005-019-0209-6).
- [31] Grasselli, F., Kampermann, H. & Bruß, D. Conference key agreement with single-photon interference. *New Journal of Physics* **21**, 123002 (2019). URL <https://doi.org/10.1088/1367-2630/ab573e>.
- [32] Carrara, G., Kampermann, H., Bruß, D. & Murta, G. Genuine multipartite entanglement is not a precondition for secure conference key agreement. *Physical Review Research* **3**, 013264 (2021). URL <http://arxiv.org/abs/2007.11553>.
- [33] Hahn, F., de Jong, J. & Pappa, A. Anonymous quantum conference key agreement. *PRX Quantum* **1**, 020325 (2020).
- [34] Grasselli, F. *et al.* Robust anonymous conference key agreement enhanced by multipartite entanglement. *arXiv:2111.05363 [quant-ph]* (2021). URL <http://arxiv.org/abs/2111.05363>.
- [35] de Jong, J., Hahn, F., Eisert, J., Walk, N. & Pappa, A. Anonymous conference key agreement in linear quantum networks. *arXiv preprint arXiv:2205.09169* (2022).
- [36] Thalacker, C., Hahn, F., de Jong, J., Pappa, A. & Barz, S. Anonymous and secret communication in quantum networks. *New Journal of Physics* **23**, 083026 (2021).
- [37] Huang, Z. *et al.* Experimental implementation of secure anonymous protocols on an eight-user quantum key distribution network. *npj Quantum Information* **8**, 1–7 (2022). URL <https://www.nature.com/articles/s41534-022-00535-1>.
- [38] Walk, N. & Eisert, J. Sharing classical secrets with continuous-variable entanglement: Composable security and network coding advantage. *PRX Quantum* **2**, 040339 (2021). URL <https://link.aps.org/doi/10.1103/PRXQuantum.2.040339>.
- [39] Dahlberg, A., Helsen, J. & Wehner, S. How to transform graph states using single-qubit operations: computational complexity and algorithms. *Quantum Science and Technology* **5**, 045016 (2020). URL <https://iopscience.iop.org/article/10.1088/2058-9565/aba763>.
- [40] Pickston, A. *et al.* Optimised domain-engineered crystals for pure telecom photon sources. *Optics Express* **29**, 6991–7002 (2021). URL <https://www.osapublishing.org/oe/abstract.cfm?uri=oe-29-5-6991>.
- [41] Fedrizzi, A., Herbst, T., Poppe, A., Jennewein, T. & Zeilinger, A. A wavelength-tunable fiber-coupled source of narrowband entangled photons. *Optics Express* **15**, 15377–15386 (2007). URL <https://www.osapublishing.org/oe/abstract.cfm?uri=oe-15-23-15377>.
- [42] Langford, N. K. *et al.* Demonstration of a simple entangling optical gate and its use in Bell-state analysis. *Physical Review Letters* **95**, 210504 (2005). URL <https://link.aps.org/doi/10.1103/PhysRevLett.95.210504>.
- [43] Dahlberg, A., Helsen, J. & Wehner, S. Transforming graph states to Bell-pairs is NP-Complete. *Quantum* **4**, 348 (2020). URL <https://quantum-journal.org/papers/q-2020-10-22-348/>.
- [44] Dahlberg, A., Helsen, J. & Wehner, S. How to transform graph states using single-qubit operations: computational complexity and algorithms. *arXiv:1805.05306 [quant-ph]* (2018). URL <http://arxiv.org/abs/1805.05306>.
- [45] Dahlberg, A., Helsen, J. & Wehner, S. The complexity of the vertex-minor problem. *arXiv:1906.05689 [quant-ph]* (2019). URL <http://arxiv.org/abs/1906.05689>.

## Appendix

### Parameter estimation

In the N-BB84 protocol QBER is defined as the largest pair-wise error rate observed from the type-1 rounds, i.e., when all users measure jointly in the Z basis. For convenience we adopt a general labelling of a group of N users following the set,  $\{A, B_1, B_2, \dots, B_{N-1}\}$ . Thus for an N-GHZ state, errors in the Z basis occur when there is a non-zero probability that one of the Bobs obtains an outcome that differs from Alice. Explicitly, the QBER is defined as:

$$\text{QBER} \doteq \max_{i \in \{1, 2, \dots, (N-1)\}} Q_{AB_i}, \quad (3)$$

where  $Q_{AB_i} = \Pr(Z_A \neq Z_{B_i}) = (1 - \langle Z^A Z^{B_i} \rangle)/2$ . As mentioned in the main text, when evaluating the pair-wise error rates for different  $i$ , the role of Alice does not have to be assigned to a specific user. Rather, we can permute the role of Alice within the set of users, by updating the indices of each user. We find different maximum pair-wise error rates (QBER) depending on the permutation, due to noise being distributed unevenly among each of the six qubits of the resource state. By iterating through all permutations, we select the role of Alice based on yielding the lowest QBER, optimising the conference key rate.

Phase error for a N-GHZ state can be estimated from X basis measurements. This is calculated by determining the deviation in measurement outcome from the expected correlations. This is expressed as,

$$Q_X = (1 - \langle X^{\otimes N} \rangle)/2. \quad (4)$$

Both QBER and  $Q_X$  are zero in the absence of error and noise, indicating that there is no deviation from the expected behaviour of the GHZ state.

For Bell states, both QBER and  $Q_X$  can be evaluated using the same expressions as above. However, since there are only two users sharing a Bell state we skip the step of permuting the role of Alice in the group.

### Experimental layout

*Photon pair sources*— To produce the six-photon graph state we use three photon-pair sources which are optically pumped by a picosecond Ti:Sapph laser. All three are type-II parametric down-conversion (PDC) sources based on domain-engineered aperiodically-poled KTP (aKTP) crystals that are optimally phase-matched for spectrally pure photon pairs at 1550 nm [40]. High spectral purity is achieved without needing narrow-band filters which improves collection efficiency and increases the overall detection rate. Each aKTP crystal is embedded in a polarisation-based Sagnac interferometer which can be optically pumped bidirectionally to produce polarisation-entangled photon pairs [41],

$$|\Psi^+\rangle_{a,b} = \frac{|hv\rangle_{a,b} + |vh\rangle_{a,b}}{\sqrt{2}},$$

where  $|h\rangle$  and  $|v\rangle$  correspond to horizontal and vertical polarisation states respectively, and subscripts denote optical modes. We remark that the  $|\Psi^+\rangle$  Bell state can be transformed into the  $|\Phi^+\rangle$  Bell state via a local operation using polarisation optics. Lastly, we can configure one of the sources to produce separable states by optically pumping the Sagnac loop in one direction, thus generating the state  $|++\rangle \doteq |dd\rangle$ , where  $|d\rangle \doteq (|h\rangle + |v\rangle)/\sqrt{2}$  is the diagonal polarisation state.

The linear optical circuit responsible for producing the six-photon graph state consists of three fusion gates [26] along with single-qubit gates on the respective modes, shown in Figure 2. The linear optical fusion gate is probabilistic, with a success rate of 1/2, however successful operation is heralded by the detection of one photon in each output of the gate. See Supplementary Methods for further experimental detail. After the network of fusion gates and upon detecting one photon in each of the six numbered modes, the joint quantum state of the system is given by,

$$|\Psi\rangle_{\text{initial}} = (|hhhhhh\rangle - |hhhhvv\rangle - |hhvvhh\rangle - |hhvvvv\rangle - |vvhhhh\rangle + |vvhhvv\rangle - |vvvvhh\rangle - |vvvvvv\rangle)/\sqrt{8}. \quad (5)$$

We remark that this state is equivalent to the six-photon graph state discussed in the main body of work, subject to

a set of local rotations,

$$(\mathbb{H} \otimes \mathbb{Z} \otimes \mathbb{H} \otimes \mathbb{Z} \otimes \mathbb{H} \otimes \mathbb{Z}) |\Psi\rangle_{\text{initial}} = |\mathbb{G}\rangle_{\text{target}}$$

where the target state is a graph state,  $|\mathbb{G}\rangle_{\text{target}}$  and  $\mathbb{H}$  is the Hadamard gate. After the fusion gates, the photons go to tomography stages which consist of a HWP, QWP and a PBS, after which photons are coupled into single mode fibres.

### Graph state formalism.

We use the graph state formalism to represent the transformations of the resource state used to distribute the GHZ state and Bell pairs between the four users. As the resource state is capable of distilling a GHZ state and sets of Bell pairs, this enables direct comparison of QCKA based on NQKD and 2QKD without changing the structure of the linear optical circuit. The general form of a graph state  $\mathbb{G} = (V, E)$  reads:

$$|\mathbb{G}\rangle = \prod_{(i,j) \in E} \text{CZ}_{ij} |+\rangle^{\otimes |V|}. \quad (6)$$

where  $\text{CZ}_{i,j}$  is the two-qubit controlled-Z gate acting on modes  $\{i, j\}$ ,  $E$  is the list of edges connecting two vertices and  $|V|$  is the number of vertices of the graph. Using this notation, we define our target graph state as,

$$|\mathbb{G}\rangle_{\text{target}} = (\text{CZ}_{1,2} \otimes \text{CZ}_{2,4} \otimes \text{CZ}_{3,4} \otimes \text{CZ}_{4,6} \otimes \text{CZ}_{5,6}) |+\rangle^{\otimes 6}, \quad (7)$$

For more details on this construction and the graph state formalism see Supplementary Methods.

One specific transformation within the graph state formalism is called local complementation (LC). An LC operation itself is comprised of two different unitaries. On a vertex designated as the target, the operation  $\text{T} = \sqrt{-i} \bar{X}_t$  is applied, whilst each vertex neighbouring the target, the operation  $\text{N} = \sqrt{i} \bar{Z}_n$  is applied.

*Measurement sequences*— After the fusion gates, each photon is sent to a tomography stage consisting of a set of controllable HWP and QWP then onto a PBS with both ports fibre coupled. From the initial target graph  $|\mathbb{G}\rangle_{\text{target}}$  LC operations are used, transforming the initial graph into alternative graphs within the same entanglement class (or graph state orbit), whereby different combinations of Bell states or a single GHZ state can be obtained [25]. This is illustrated in Figure 2 in the main text.

We assign Alice, Bob-1, Charlie, Debbie, Bob-2 and Bob-3, to qubit numbers 1, 2, 3, 4, 5 and 6 respectively. To evaluate the AKR for a comparison between QCKA techniques, we need to calculate  $Q_Z$  and  $Q_X$  for each state that plays a part in the QCKA protocol. The smaller resource states users require for QCKA are not directly obtained from the initial graph state. Instead, necessary single-qubit operations applied to the initial graph—to obtain the required graph—are encoded onto the measurements settings that network users would otherwise have used. Obtaining a GHZ shared between Alice and the Bobs in the four-photon state space, to carry out QCKA with a multi-partite resource, Charlie and Debbie are required to make projections in the Z basis. So for each round of measurements, whilst Charlie and Debbie should always measure in the Z basis, Alice and the Bobs measurements are made based on whether they want to complete a type-1 round or type-2 round of the protocol. For example, to measure the observable  $\langle Z_1 Z_2 Z_5 Z_6 \rangle$  of the GHZ state to evaluate the QBER, all users must measure the observable  $\langle Z_1 Z_2 X_3 X_4 Z_5 Z_6 \rangle$ , where the required single-qubit operations leave the default measurement settings unchanged for Alice and the Bobs, but rotate Charlie and Debbie's measurement settings. To measure the observable  $\langle X_1 X_2 X_5 X_6 \rangle$  of the GHZ state to obtain  $Q_X$ , all network users must measure the observable  $\langle X_1 Y_2 X_3 X_4 X_5 Y_6 \rangle$ , where now single-qubit operations encoded onto the measurement settings correspond to rotations of measurements into a different basis. When Alice and the Bobs wish to partake in QCKA with bi-partite resources, the measurement procedure suitably follows that of the GHZ state, except now the observables are for Bell states, and alternate single-qubit—based on required rotations applied to the initial graph—are encoded onto these settings. Full blueprints containing the operations applied to each qubit within each measurement set are presented in Figure 2. The measured  $\langle Z^{\otimes N} \rangle$  and  $\langle X^{\otimes N} \rangle$  observables, where N is the qubit number, of the three Bell states and the GHZ state used in this protocol are presented in Figure 3.

## Supplementary Materials

## Supplementary Methods

Here we outline how the six-qubit graph state in the experiment is mapped from the graph notation onto the linear optical circuit shown in Fig. 4. From the mathematical description of a graph (Equation 6 in the Appendix of the main text) one can see that to prepare a graph state requires  $V$  qubits initialised as  $|+\rangle$  (equivalent to  $|d\rangle$  in polarisation encoding), connected via CZ gates between specific qubits classified by  $E$ . The graph state generated in this work can be mapped onto a general circuit model depiction which consists of six qubits initialised in  $|+\rangle$  and five CZ gates. Directly translating the circuit model depiction into an experimentally realisable linear optical circuit leads to large inefficiencies. Realising CZ gates with linear optics results in a low probability of success of  $1/9$  per gate [42]. Instead, we found a linear optical circuit that could produce a state equivalent to the targeted graph state (up to local rotations) based on linear optical fusion gates, which have a much higher probability of success of  $1/2$ . Explicitly realising this linear optical circuit does require some entangled resources, namely two Bell pairs as well as a pair of separable photons. Three linear optical fusion gates are then used to generate multi-photon entanglement, producing the desired state. Finding the translation to a linear optical circuit enabled the investigation in this work, as the general circuit model approach carries a probability of success of  $1/59,049$ . Our arrangement has a probability of success of  $1/8$ .

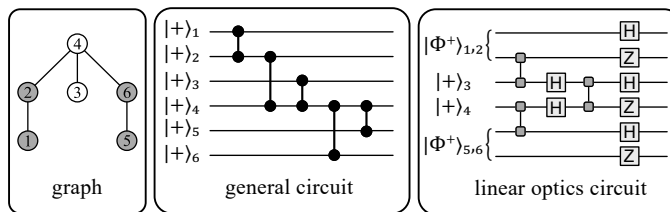


FIG. 4. **Graph representation and its realisation.** The 6 qubit graph state in our experiment is shown in the left panel. This can be translated into a generalised quantum circuit depicted in the middle panel. Our setup, which is more experimentally friendly in linear optics, is shown in the right panel. Notably we employ Bell states,  $|\Phi^+\rangle$  and replace the two-qubit CZ gates with fusion gates. Additional single qubit operations, Hadamard and Pauli-Z gates are needed to correct the final state.

We generate photon pairs using type-II parametric down-conversion (PDC) sources that operate in the filter-less regime, owed to the fact we employ domain engineering techniques to modify the phase-matching function (PMF) of the down-conversion process. Despite our aperiodically poled KTP (aKTP) crystals operating without filters, two-photon interference visibilities of up to  $98.6 \pm 1.1\%$  are still obtainable, meaning we carry forward minimal errors after any instances of two-photon interference. Without lossy spectral filters we can also access heralding efficiencies of up to  $67.5\%$  [40].

We use a pulsed Ti:sapph laser with a central wavelength of  $774.9\text{nm}$  producing photon pairs in a degenerate condition at  $1549.8\text{nm}$ . These wavelengths were chosen to keep the crystal temperatures sufficiently far away from room temperature. This laser operates with a pulse duration of  $1.3\text{ps}$ , matching the pump-envelope function (PEF) bandwidth to the PMF bandwidth at a repetition rate of  $80\text{MHz}$ .

For generating Bell states, we place our PDC sources inside a Sagnac interferometer, where a pump photon generates signal and idler pairs in either a clockwise or anti-clockwise direction depending on the polarisation state of the pump photon. When the pump photon is equally likely to produce photons in the clockwise direction and the anti-clockwise direction an entangled state is generated. This configuration explicitly consists of a Glan-Taylor prism, which ensures the pump is in a linear polarisation state followed by a HWP which rotates this linear polarisation state into  $|d\rangle$  for generating an entangled state, or a linear basis state for generating a separable state. After the pump polarisation state is prepared, it is transmitted through a dichroic mirror (DM) which only reflects the down converted photons propagating back towards the pump. The pump is then probabilistically split on a dual-wavelength polarising beam-splitter (dPBS) into transmitted or reflected spatial modes. In the transmitted mode, the pump photon is in the  $|h_p\rangle$  polarisation state and will generate signal and idler pairs in a clockwise direction. In the reflected mode, the pump photon is rotated from  $|v_p\rangle$  into  $|h_p\rangle$  by a dual-wavelength HWP (dHWP) to facilitate type-II PDC in the anti-clockwise direction. When photons are generated from a pump photon in the transmitted mode of the dPBS, the down-converted pair are each rotated by the dHWP, which acts to fix the temporal offset the different set of photon pairs possess, before being split by the dPBS and collected into SMFs [41]. Upon collection, the signal and idler pairs

exist in a maximally entangled state

$$|\Psi^-\rangle = \frac{1}{\sqrt{2}} |h_s v_i\rangle - e^{i\phi} |v_s h_i\rangle.$$

To generate the six-photon state presented in this work, we prepare two Bell states as  $|\Phi^+\rangle$  (which are equivalent to  $|\Psi^-\rangle$  up to local rotations) in modes  $\{1, 2\}$  and  $\{5, 6\}$  and a single separable state prepared as  $|\text{dd}\rangle$  in modes  $\{3, 4\}$ . We employ linear plate polarisers (LPPs) to prepare the state  $|\text{dd}\rangle$ . The required unitaries for Bell state preparation are performed with manual fibre polarisation controllers (FPCs). These unitaries act between the sources and fusion gates. The fusion gates consist of imposing two input optical modes, launched from SMFs, onto a PBS. Each output modes of the PBS are then collected into SMFs. A successful fusion operation occurs when there is one and only one photon in each output optical mode. This means that for the full circuit to be successful, only a single photon should be in the six optical modes after the three fusion gates. Within each fusion gate there are additional optics to correct for the local phase that the PBS within each of these gates introduces. The correction optics are made up of a HWP sandwiched between two QWPs. Fusion gate 1 ( $F1$ ) acts between modes  $\{2, 3\}$ , fusion gate 2 ( $F2$ ) between  $\{4, 5\}$  and finally, fusion gate 3 ( $F3$ ) acts between one of the outputs of both  $F1$  and  $F2$ , in modes  $\{3, 4\}$ . The only difference between these gates is the presence of an additional HWP, just before the PBS within  $F3$ , which is present to apply a single-qubit Hadamard gate. Final FPCs situated directly after the fusion gates ensure that photons undergo an identity operation between the fusion gates and measurement. Only the detection of a six-fold event (six photons arriving individually across all six optical modes comprised of daughter PDC photons created from the same pump pulse train) heralds the success of all three fusion gates, even in our case where the outputs of  $F1$  and  $F2$  feed directly into the input of  $F3$ .

The final part of the circuit is comprised of measurement stages which consist of a QWP, HWP and PBS. These stages perform projective measurements. The measured photons are detected using superconducting nano-wire single photon detectors that operate at quantum efficiencies  $> 80\%$  at our wavelengths. Detection events are processed by time-tagging logic. A full schematic of the experimental arrangement can be seen in Figure 6.

All rotations required to allow Alice and Bobs to share different resource states among them are encoded onto the measurement settings. Figure 5 is an example of the experimental arrangement for a round in which Alice and the Bobs wish to share a GHZ state. The single-qubit operations acting on each mode after the creation of the resource state, highlighted in yellow and orange within Figure 5, are applied to each qubit upon measurement, meaning that each user is provided with measurement settings required to extract different states from the shared network resource state. In this way, entanglement amongst a subset of the six network users can be allocated in a dynamic way. To determine the correct measurements users have to perform, we first decide which type of measurement round being performed, either type-1 or type-2. For both measurement types we already know that Charlie and Debbie, modes  $\{3,4\}$ , are required to measure in the Z-basis, so operations on their qubits are encoded onto their measurement basis. Settings on Alice and Bobs qubits, or modes  $\{1,2,5,6\}$ , do depend on which type of round is being performed. If a type-1 round is taking place, then their starting measurement basis is Z, and the single qubit operations on that

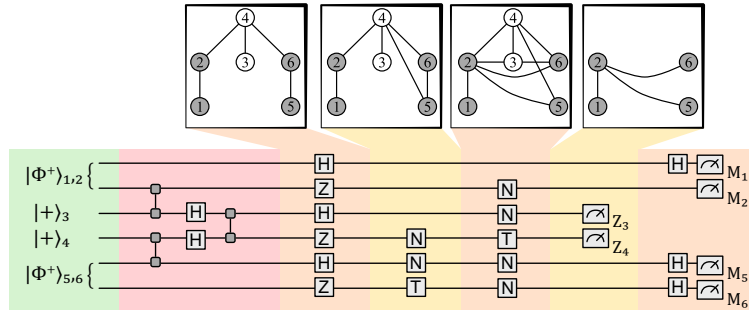


FIG. 5. **Generating and manipulating the 6-photon graph state.** We prepare the 6-photon graph state using photon-pair sources and a linear optics scheme. Two of the sources are prepared in the Bell state,  $|\Phi^+\rangle$ , while the third is in a biseparable state with each photon in  $|+\rangle$  as shown in the green region. Using three Fusion gates and single-qubit rotations one arrives at the 6-photon graph state, up to a set of local rotations, as shown in the red region. The set of graph transformations for obtaining the 4-qubit GHZ state, in modes  $\{1, 2, 5, 6\}$ , is shown in the two-tone orange shaded regions. Notably these consist of local operations and quantum measurements on non-participatory qubits  $\{3, 4\}$  in the Z basis.

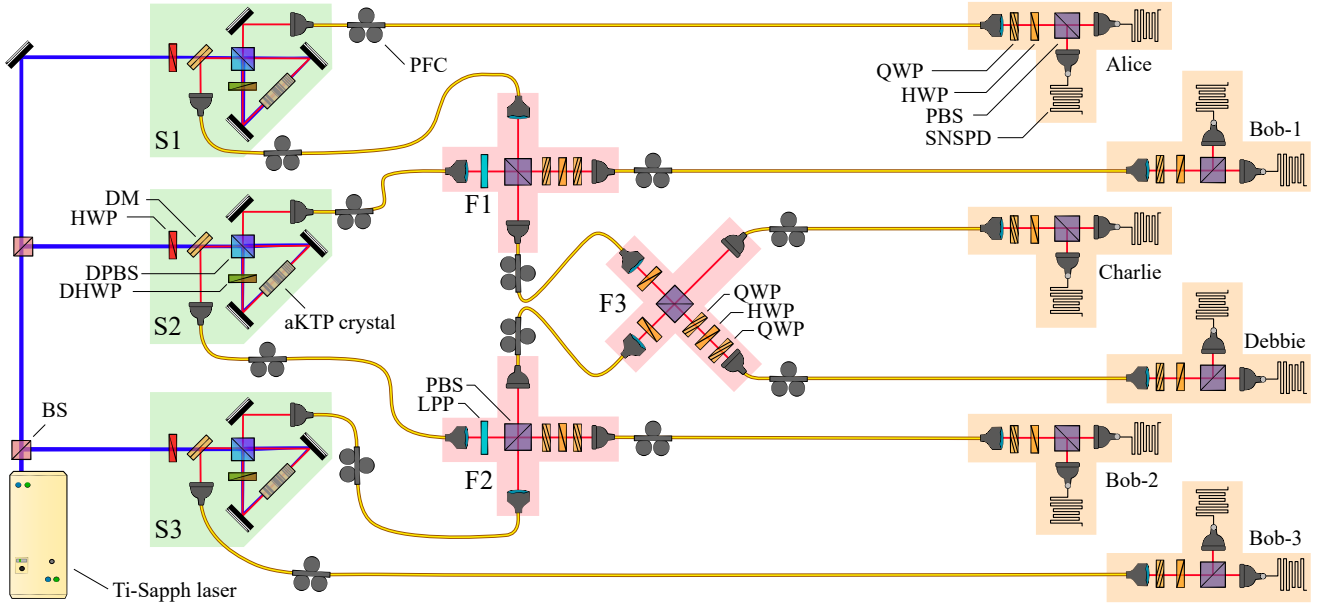


FIG. 6. **Experimental layout.** Highlighted in green are the sources, linear optical Fusion gates are in red and polarisation projective measurement stages in orange. Each source consists of an aKTP crystal, pumped by a Ti-Sapph laser and embedded in a Sagnac loop with a HWP to set the pump direction. Note only sources  $\{S1, S3\}$  are entangled while  $S2$  is pumped in one direction to produce biseparable states. Each photon is coupled into single-mode fibre with fibre polarisation controllers (PFC) used to set the desired polarisation states entering the Fusion gates  $\{F1, F2\}$ . Additionally, photons from  $S2$  are sent through linear plate polarisers (LPP) to initialise their states in  $|+\rangle$ . Each Fusion gate comprises of two input optical modes which overlap on a polarising beam splitter (PBS) and successful operation of the two-qubit gate is conditional on one photon in each output mode. In each Fusion gate a HWP sandwiched by two quarter-wave plates (QWP) is used to compensate local phase shifts introduced by the PBS. In the final Fusion gate  $F3$ , two HWPs are used to apply the single-qubit Hadamard gates. The remaining single-qubit gates are determined by the protocol and implemented in the projective measurement stages on each qubit which consist of a QWP, HWP and PBS. Single photons are detected using superconducting nanowire single photon detectors (SNSPDs).

mode are applied to rotate (or leave unchanged) this measurement basis. Likewise for type-2 rounds. Hence, as shown in the Appendix section, the measurement  $\langle Z_1 Z_2 Z_3 Z_4 Z_5 Z_6 \rangle$  to complete a type-1 round actually requires the measurement  $\langle Z_1 Z_2 X_3 X_4 Z_5 Z_6 \rangle$  after rotation have been applied, and the measurement  $\langle X_1 X_2 Z_3 Z_4 X_5 X_6 \rangle$  becomes  $\langle X_1 Y_2 X_3 X_4 X_5 Y_6 \rangle$ . As a consequence of the GME implicit of the shared network resource state, whenever Charlie and Debbie perform a measurement they need to disentangle themselves from the system coherently. When Charlie and Debbie measurements are in the X basis (due to rotations), they can attain either 0 or 1 as their result. The resulting GHZ may contain a local phase rotation conditioned on the outcomes of Charlie and Debbie. This rotation must be corrected for and is done so in a post-processing step.

The work contained within this manuscript focuses on an investigation into a network protocol, where the particular scenario demands the distribution of a GHZ and a number of Bell states to specific users. For the determining how to obtain states, we use a software library which can manipulate graph states based on available experimental transformations. This lets us form a search of available smaller resource states a given graph can produce. The search is brute-force, emanating from the fact that transforming graphs, or more generally stabilizer states, into tensor products of bipartite Bell pairs, or just a set of Bell pairs between specific vertices, using only a certain class of local operations and classical communication is a NP-complete problem [43]. Likewise for GHZ state distillation from arbitrary graphs, if we wish to arrive at a GHZ state between a specific set of vertices [44] or if we require a GHZ state of fixed size [45], the task is NP-complete.

### Supplementary Results

Assessing the performance of the protocol at a variety of different six-photon generation rates, reveals how the rates scale with noise. The main source of noise that degrades the quality of the prepared state is from higher order photon

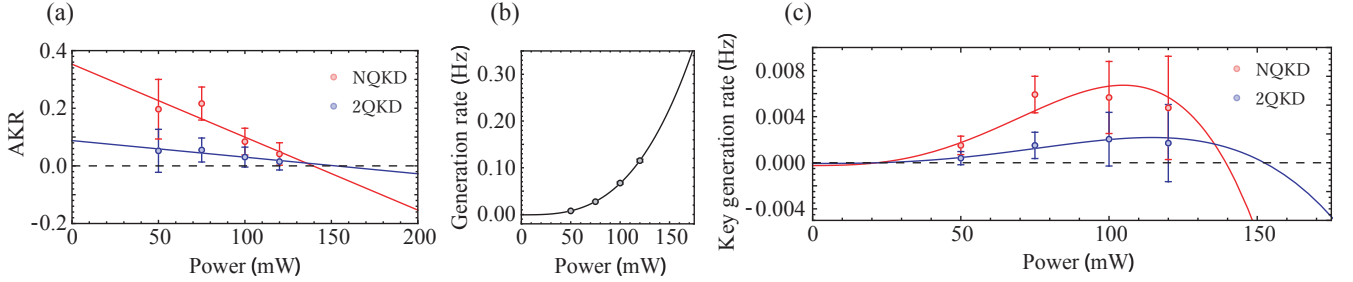


FIG. 7. **AKR, raw photon generation rate and key generation rate as a function of the pump power.** Multi-photon generation rate from a PDC source is not linear with respect to the amount of optical pump power applied to the non-linear crystal. The benefit of having higher pump powers is a larger  $N$ -fold generation rate. A caveat to this relationship is the additional noise generated by the presence of  $> N$  photons consequential of the probabilistic nature of the PDC sources. (a) Shows how the AKR becomes worse as the pump power increases, a direct result of the additional noise present when higher order photon pairs are produced. (b) The  $N$ -fold generation rate however, follows a cubic increase. This means that although the noise increases as a function of power, the generation rate increases quicker than the noise decreases. (c) The key generation rate is a product of both the AKR and the generation rate, revealing that for the experimental parameters contained within this work, the ideal pump power is  $\sim 105\text{mW}$  in order to obtain the highest key generation rate with an NQKD approach to QCKA.

pair emissions due to the probabilistic nature of PDC sources. Even whilst operating with a post-selection criteria, higher order emission events can trigger detection patterns identical to that of the signal. These higher order emission terms result in a reduction to the magnitude of coherence, as events from incorrect pair generation events interfere with signal photons and degrade the purity of the state. The relation between the overall noise and the AKR is not trivial, partly due to the fact noise is not symmetrically distributed across the quantum state. This is evidenced by the different QBER and  $Q_X$  for each of the Bell states derived from the same resource state. To attain the highest possible key generation rate, a power dependence measurement is required. This will reveal the ideal power to operate the protocol at. By computing the product of the AKR, which will fall with respect to an increase in pump power, and the raw photon generation rate, which will increase as a function of the pump power, the key generation rate can be calculated. Figure 7 presents the scaling of AKR, generation rate and ultimately the key generation rate as a function of pump power, revealing that the highest key generation rate is at  $\sim 105\text{mW}$ .

### Supplementary Discussion

We remark that owing to the non-deterministic operation of the fusion gates and photon sources in this experiment, all six users must detect a single photon in their measurement stages to obtain the correct graph state. It would be an interesting prospect to determine whether this graph state inherits any loss robustness for the purposes of QCKA, or indeed other applications when deterministic sources and gates are used to generate them. Starting from  $|\mathcal{G}\rangle_{\text{initial}}$ , to achieve two Bell states between  $\{1, 2\}$  and  $\{5, 6\}$  all that is required—in principle—is a single  $Z$  basis measurement on qubit 4, tolerating the loss of qubit 3 and still adhering to the graph state formalism.

In this work, we chose to generate the resource graph state  $|\mathcal{G}\rangle_{\text{initial}}$  based on its accessibility with probabilistic photon sources and linear optical components. If we had generated a  $N$  qubit GHZ state and distributed this amongst network users, the rate advantage for NQKD scales as  $N - 1$ . We however, showed a rate advantage for the NQKD approach which did not scale as  $N - 1$ , but a rate advantage of a factor of two, due to the ability to multi-cast Bell pairs from the shared resource state. Interestingly, there are families of graph states where the rate advantage can be reduced even further. In a similar scenario to the work in the main text, the ring graph is capable of distributing a GHZ state and Bell states to network users. Using the ring graph as a network resources can allow users to cast pairs of Bell states in *every* round, differing from the graph used for investigations within this work. Because of this, there is more contribution to the overall key per network usage due to more pair-wise key distribution within the 2QKD rounds. Figure 8 shows the operations required to obtain smaller network resources from the ring graph state. Like in the main text, all operations are either local rotations or single-qubit projection measurements.

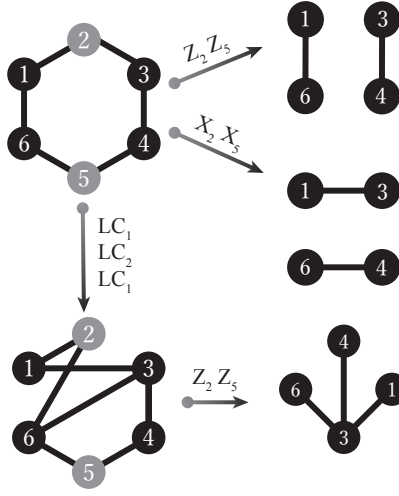


FIG. 8. **Ring graph state and the operations required to obtain smaller network resource states.** The ring graph can be used in a similar means to  $|\mathcal{G}\rangle_{\text{initial}}$  to compare the key rates of different approaches to QCKA. Four users—in this illustration  $\{1,3,4,6\}$ —are designated as the network users. These four users can attain pair-wise correlations with each other upon the application of Z measurements or X measurements by the two remaining users. To obtain a GHZ state, local complementation operations are required, followed by the application of Z measurements, again performed by the non-participating members of the communication protocol.